Article

Microcrystal Electron Diffraction for Molecular Design of Functional Non-Fullerene Acceptor Structures

Steve Halaby, Michael W. Martynowycz, Ziyue Zhu, Sergei Tretiak, Andriy Zhugayevych,* Tamir Gonen,* and Martin Seifrid*

Read Online

ACCESS | Metrics & More | Article Recommendations | Supporting Information

ABSTRACT: Understanding the relationship between molecular structure and solid-state arrangement informs about the design of new organic semiconductor (OSC) materials with improved optoelectronic properties. However, determining their atomic structure remains challenging. Here, we report the lattice organization of two non-fullerene acceptors (NFAs) determined using microcrystal electron diffraction (MicroED) from crystals not tractable by X-ray crystallography. The MicroED structure of o-IDTBR was determined from a powder without crystallization, and a new polymorph of ITIC-Th is identified with the most distorted backbone of any NFA. Electronic structure calculations elucidate the relationships between molecular structures, lattice arrangements, and charge-transport properties for a number of NFA lattices. The high dimensionality of the connectivity of the 3D wire mesh topology is the best for robust charge transport within NFA crystals. However, some examples suffer from uneven electronic coupling. MicroED combined with advanced electronic structure modeling is a powerful new approach for structure determination, exploring polymorphism and guiding the design of new OSCs and NFAs.
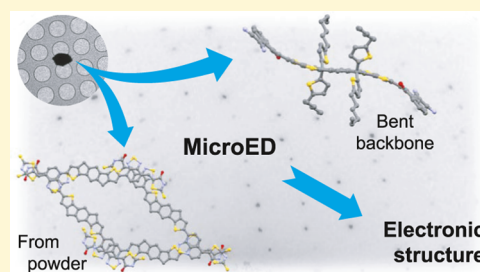
INTRODUCTION

Organic semiconducting materials are a topic of interest across a range of scientific and engineering disciplines due to their potential integration within emerging optoelectronic devices, including organic light-emitting diodes (OLEDs), organic field-effect transistors (OFETs), and organic photovoltaics (OPV).[1] Organic semiconductors (OSCs) are particularly attractive due to their tunable properties through versatile molecular design and synthesis, their amenability to solution deposition techniques, and their compatibility with lightweight and flexible substrates.[1] Modification of the molecular structure can be used to tune energy levels, charge carrier transport, optical absorbance, solubility, and solid-state organization.[2–4] For example, fabrication of device active layers processed from organic solvents can be achieved through the addition of pendant alkyl chains attached to the π-conjugated backbones of molecular and polymeric OSCs. The optical properties and energy levels of OSCs can be manipulated by introducing subunits that vary in their degree of electron-donating or -accepting ability during the synthesis of the molecules.

In the OPV field, this design strategy has been effectively employed to improve the performance of the electron-donating materials, hundreds of which have been reported.[5,6] In contrast, the dominant electron-accepting materials in high-performing OPV devices have been traditionally based on C_{60} or C_{70} fullerene cages, which are poorly amenable to diverse synthetic modifications.[7] The most successful fullerene

derivatives, [6,6]-phenyl-C_{61}-butyric acid methyl ester ($PC_{61}BM$) and [6,6]-phenyl-C_{71}-butyric acid methyl ester ($PC_{71}BM$), are rendered solution-processable by the addition of a phenyl ring and butyric acid methyl ester to the fullerene cage. Further synthetic modification has proven difficult, especially precluding attempts to improve the poor optical absorbance of fullerene derivatives.[7] Recently, the need for alternatives to fullerene-based materials has become clear as power conversion efficiencies (PCEs) of devices incorporating these materials as the electron-accepting component stagnated at ca. 11% for single-junction OPV devices.[8]

High-performing non-fullerene acceptor (NFA) materials have substantially revitalized interest in OPVs. Progress in molecular design, characterization, and device fabrication using NFAs has resulted in PCEs as high as 18.2%.[9,10] The molecular design and synthesis approach developed through the study of OPV donor materials can be translated to this new class of NFAs to tune their optoelectronic properties, resulting in rapid progress.[11] Current high-performing NFAs are described by a planar conjugated backbone composed of a central electron-rich donor core flanked by strongly electron-withdrawing
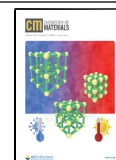
acceptor units. Attached to the donor moiety are bulky solubilizing chains, usually connected to the π-conjugated backbone by an sp[3]-hybridized bridging atom, which results in 3D steric bulk out of the plane of the backbone. Results of simulations and crystal structure characterizations obtained from X-ray diffraction (XRD) indicate that the molecular architecture of NFAs can result in a 3D network of intermolecular contacts and charge carrier transport that is potentially similar to that present in fullerenes.[12−21]

To fundamentally understand the elements of NFA chemical structure that result in their functional properties, it is necessary to experimentally determine their organization in the solid state. Intermolecular interactions define properties important to device performance, such as orbital overlap, electronic coupling, charge carrier mobility, and optical absorbance.[22] From the solid-state organization, it is possible to calculate electronic structure and provide a more fundamental explanation for the properties and device performance of NFA materials.[14,20,23] Such progress, however, is hampered by difficulties in obtaining single crystals of sizes suitable for X-ray diffraction experiments.

Recently, a technique that may make determining the single-crystal atomic structure of molecular semiconductors more easily achievable has been described in the literature.[24,25] The cryogenic electron microscopy (cryoEM) technique of micro-crystal electron diffraction (MicroED)[24] originated in the field of structural biology, where it was successfully used to determine the 3D structures of biological macromolecules previously unattainable via traditional X-ray diffraction techniques.[26−32] MicroED enables the determination of atomically resolved structures from crystals that are a billionth the size that is needed for X-ray diffraction. Furthermore, it has recently been demonstrated that MicroED can be used to easily solve the structure of organic molecular solids.[33,34] Recent reports have also demonstrated this and other electron diffraction methods for understanding the microstructure of thin films of OSCs.[35−37] MicroED has tremendous potential in the field of OSC research—especially for solution-processable molecules, as it opens up the possibility for robust determination of the atomic structures of materials that have so far been difficult to study.

In this study, we used MicroED to determine the atomic structures of two commercially available NFAs. Specifically, ITIC-Th[38] and o-IDTBR[39] are well-known electron-accepting components in high-performing OPV devices. Notably, the MicroED structure of o-IDTBR was determined from microcrystals directly from a commercially available powder, which reduced the effort required for structure determination. We find that both molecules form 3D networks in the solid, although their packing is significantly different. The conjugated backbones in the o-IDTBR crystal form a "three-dimensional (3D) wire mesh" made up of four molecules, surrounding an insulating channel made of solubilizing octyl chains. In the case of ITIC-Th, the 3D network is achieved by a more complex set of arrangements, involving two distinct conformers, both of which are significantly more distorted than typically assumed for electronically delocalized molecular frameworks. The ITIC-Th MicroED structure has the most contorted NFA backbone reported so far, which raises questions about our under-standing of the rigidity of fused-ring conjugated systems and the discovery of possible OSC polymorphs. The latter is particularly important since little is known about poly-morphism in OSCs outside of a small number of well-studied

materials. Modern density functional theory (DFT) methods are applied to the atomic structures determined from MicroED, as well as to similar NFAs reported in the literature. Analyzing and comparing the calculated electronic structures to other known crystals are used to understand the impacts of molecular packing and lattice topology on charge transport.

RESULTS AND DISCUSSION

Atomic Structures Determined by MicroED. The atomic structure of o-IDTBR (molecular structure in Figure 1a) was determined by MicroED to a resolution of 0.9 Å
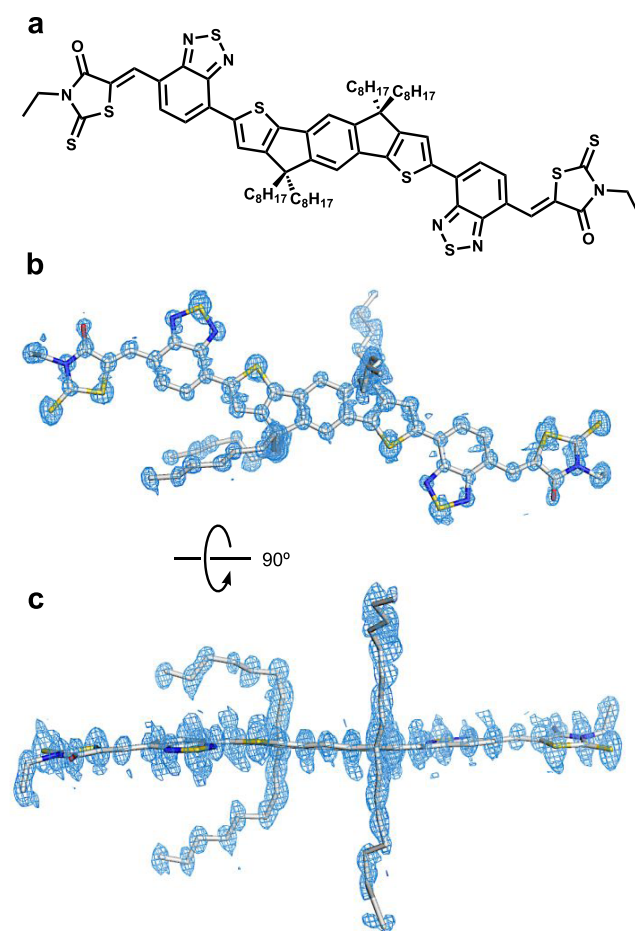

Figure 1. Molecular and MicroED structures of o-IDTBR. Molecular structure of o-IDTBR (a), density maps and 0.9 Å resolution structure of o-IDTBR determined by MicroED as viewed normal to the plane of the backbone (b) and in the plane of the backbone (c) to highlight the orthogonal arrangement of the octyl chains. Maps are 2mF₀−dF_c maps contoured at the 1.5σ level with a 2 Å carve for clarity. The arrow represents the 90° rotation of the crystal around the given axis.

(Figure S1 and Table S1) from a powder without prior purification or crystallization. Figure 1b,c shows the density maps determined by MicroED. The MicroED structure of o-IDTBR is similar to that previously reported from X-ray crystallography (Figure S2),[17] which indicates that MicroED is a suitable alternative for solid-state structure determination of OSC molecules. The π-conjugated backbone is relatively planar, with the solubilizing octyl chains oriented orthogonal to the plane of the backbone (Figure 1c). Intramolecular S···N short contacts between the indacenodithiophene and benzo-thiadiazole heterocycles act as a planarity lock. Intramolecular
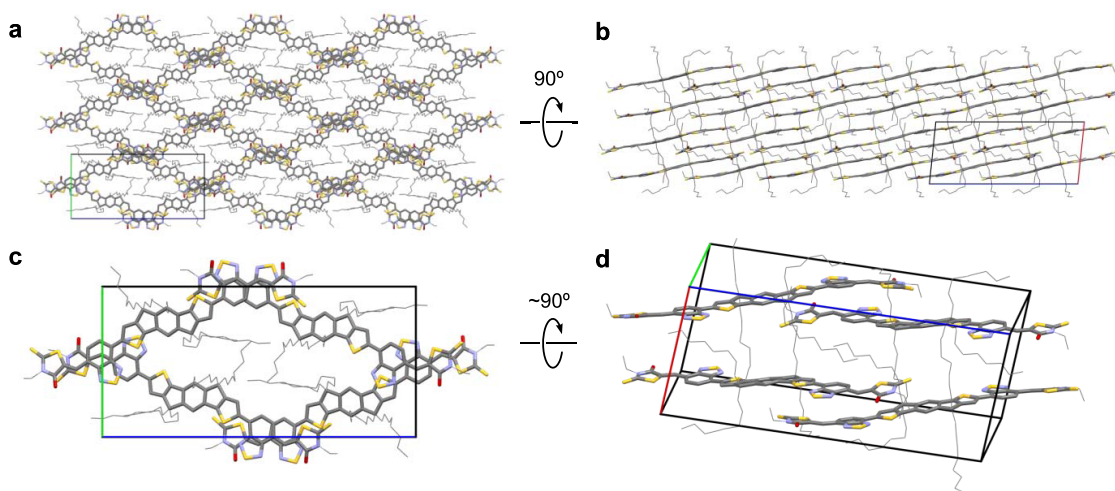
Figure 2. Lattice of o-IDTBR determined from MicroED. Views of the o-IDTBR MicroED structure along the *a*-axis (a) and the *b*-axis (b) of the unit cell. View of four o-IDTBR molecules that form a parallelogram in the 3D wire mesh (c). Side view of the same parallelogram to emphasize the lack of direct contact between molecules at an acute angle (d). Hydrogens are omitted for clarity, and alkyl chains are depicted as wireframe structures. The red, green, and blue axes correspond to the *a*, *b*, and *c* axes of the unit cell, respectively. The arrows represent a 90° rotation of the crystal around the given axis.

left−right (L−R) symmetry is broken by crystallographic symmetry. The left (L) and right (R) sides of the o-IDTBR ground-state geometry in vacuum calculated by DFT are the same because of the molecule's inversion symmetry. However, analysis of the MicroED structure (Figure S3) shows that it is asymmetric with respect to all elements of $P2_1/c$ symmetry. There are differences between the L and R sides due to differences in their local interatomic packing in the crystal: the backbone is very planar on the L side but slightly twisted on the R side.

The o-IDTBR molecules pack in a wire mesh defined by the backbones, with channels for the insulating alkyl chains, as seen in Figure 2a,b. Interlayer contacts occur through $\pi\cdots\pi$ stacking between the benzothiadiazole and rhodanine acceptor units (Figure 2c). There are no direct intermolecular contacts between two molecules at an acute angle relative to each other (Figure 2d). Instead, there are only three types of intermolecular contacts (Figure 3): obtuse (LR/RL), parallel-close (RR), and parallel-far (LL). All three contact types involve various degrees of $\pi\cdots\pi$ stacking and short contacts between octyl chain hydrogens and polar carbonyl or thiocarbonyl groups. The backbones of the molecules in RR (Figure S4a) and LL (Figure S4b) contacts form a slipped stack, while the backbones of the LR/RL contact (Figure S4c) are at a ~139° angle. Typical $\pi\cdots\pi$ stacking distances of 3.3–3.6 Å are observed. Short intermolecular contacts between the octyl hydrogens of one molecule and the carbonyl oxygen or thiocarbonyl sulfur atoms likely serve to stabilize the structure.

Formation of a 3D packing network through the overlap of the acceptor units—the primary location of the lowest unoccupied molecular orbital—hints at relevance for o-IDTBR's success as an acceptor material in OPV devices.[40] The 3D wire mesh topology is anticipated to favor charge migration through a given layer, and hopping between layers occurs through the acceptor–acceptor contacts at the nodes of the wire mesh.

The MicroED structure of ITIC-Th (molecular structure in Figure 4a), referred to as *β*-ITIC-Th, was determined to a resolution of 1.0 Å (Figure S5 and Table S1). The π-
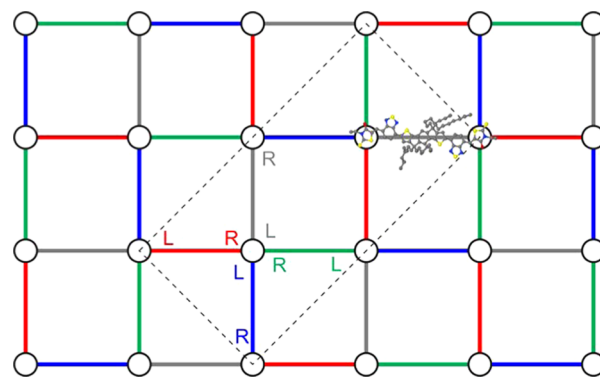

Figure 3. "Wire mesh" topology of electronic connectivity in the o-IDTBR lattice. The π-stacking direction is perpendicular to the plane shown here. Colored sticks denote molecules: each color corresponds to a single layer parallel to the (201) crystallographic plane. There are four layers in the unit cell marked by red, green, blue, and gray colors from top to bottom, respectively. The unit cell within the plane is shown by the dashed rectangle. All molecules are symmetry equivalent and have no central symmetry due to the low symmetry of the lattice, so they have left (L) and right (R) ends. Intermolecular contacts in a π-stack are marked by disks. There are three symmetry-nonequivalent contacts: RR, LL, and RL = LR. Because one of the electronic couplings in o-IDTBR is four times smaller than the other two, the 3D connectivity is not perfect. If two couplings are broken, there will be no connectivity at all since the 2D mesh in each layer itself is disconnected and becomes connected in 3D only when all such 2D layers are π-stacked.

conjugated backbones of the molecules are significantly less planar than typically expected for OSC materials in the solid state. There are two different conformers of ITIC-Th within the lattice: highly contorted (HC, Figure 4b,c) and less contorted (LC, Figure 4d,e). The commonly assumed S···O intramolecular short contacts between the sulfur of the indacenodithienothiophene (IDTT) unit and the oxygen of the indanone-malononitrile (IC) unit are observed in both conformers (Figure S6), giving evidence that the S···O interaction is an effective intramolecular lock.
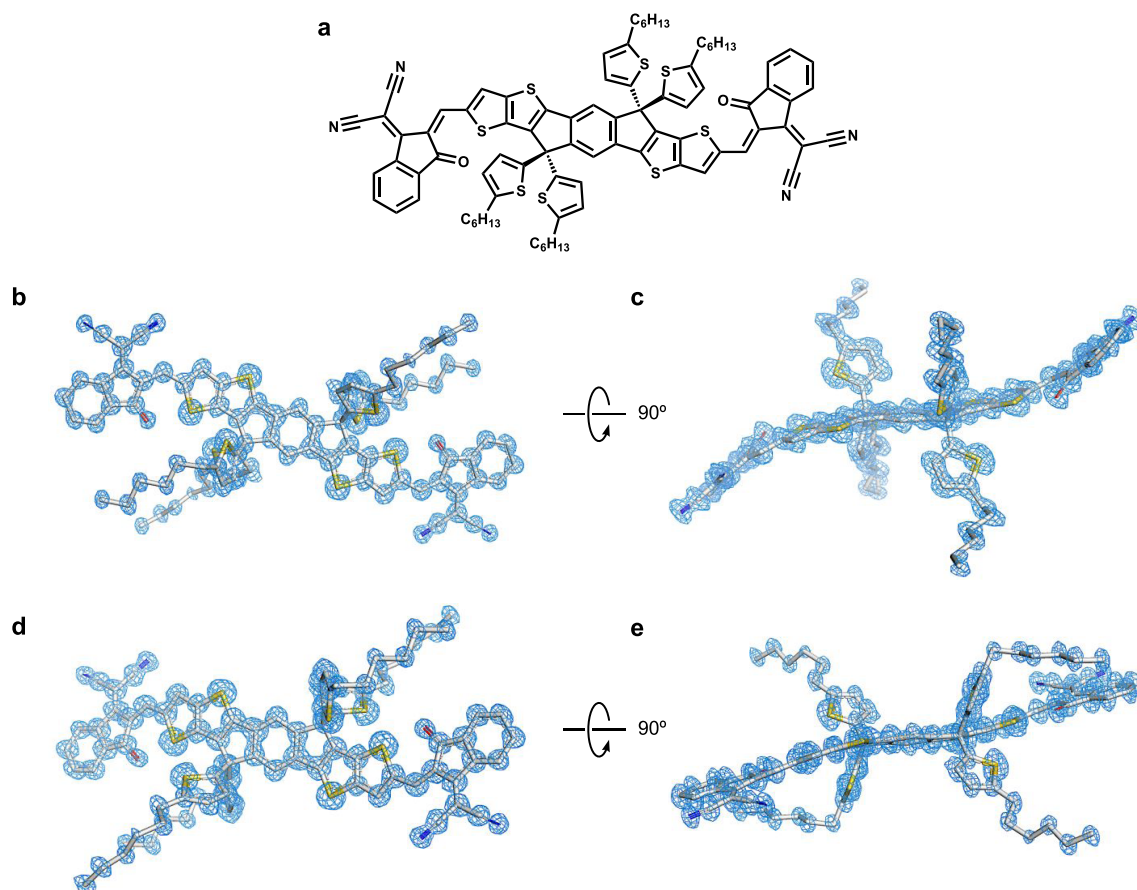
Figure 4. Molecular and MicroED structures of ITIC-Th. Molecular structure of ITIC-Th (a) and density maps of two different conformers of β-ITIC-Th determined using MicroED: the HC conformer (b, c) and the LC conformer (d, e). Maps are $2mF_o-dF_c$ maps contoured at the 1.5σ level with a 2 Å carve for clarity. The arrows represent a 90° rotation of the crystal around the given axis.

The β-ITIC-Th structure constitutes the most distorted NFA backbone reported to date. The outer thiophene ring of the HC IDTT core is bent out-of-plane at an angle of 19.2° (Figure 5a) relative to the central phenyl ring (backbone bend), while the IC unit is bent out-of-plane at an angle of 47.4° (end-group bend). The outer thiophene ring of the LC IDTT core is at a 16.7° angle (Figure 5b) relative to the central phenyl ring, while the IC unit is at a 22.1° angle. There are only three X-ray crystal structures reported in the literature with noticeable backbone bending: β-ITIC,[12] 4TIC,[13] and R10-4Cl[15] (molecular structures in Figure S7). However, none of their backbones are as distorted as β-ITIC-Th. The largest backbone bend is in the R10-4Cl crystal (11.3°),[15] while the largest end-group bend is in β-ITIC (34.7°).[12] It should be noted that out-of-plane bending typically corresponds to the lowest vibrational mode of elongated, planar π-conjugated molecules (not counting possible dihedral librations with imaginary frequencies). In particular, if we replace the side chains of the ITIC-Th molecule with hydrogen atoms and relax the geometry, the resulting conjugated backbone will be planar with the smallest frequency of 6 cm^{-1} corresponding to the out-of-plane bending and the third smallest frequency of 16 cm^{-1} corresponding to the higher-order out-of-plane bending, as shown in Figure 5. Moreover, the second smallest frequency at 9 cm^{-1} corresponds to the rotation of end groups, as shown in Figure 5. The energy of such deformations is small compared to intermolecular interaction energies.[41] Many nonplanar conjugated molecules such as polythiophenes and
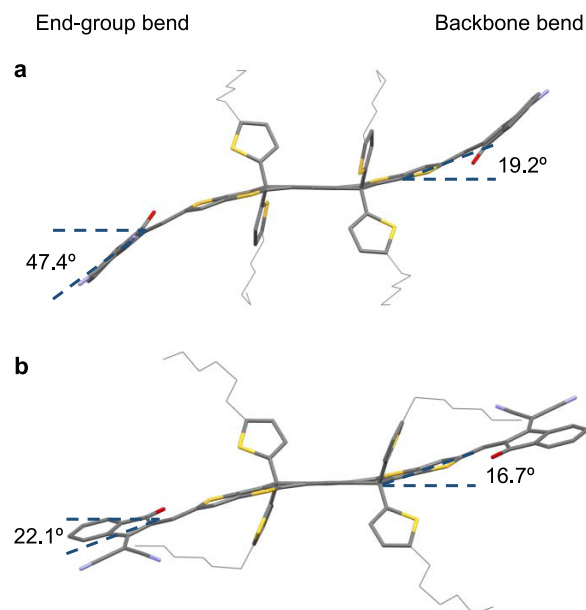
End-group bend   Backbone bend

Figure 5. Out-of-plane bending angles of the (a) HC conformer and (b) LC conformer. Backbone bending is represented on the right of the molecule, while end-group bending is represented on the left. Hydrogens are omitted for clarity, and alkyl chains are depicted as wireframe structures.

polyphenylene-vinylenes, which have a very small planarization energy penalty, also become planar in their crystalline forms.[42−45] However, they do not possess the same fused-ring backbone structure. Understanding the origins and consequences of such a distorted backbone is important for understanding the solid-state and electronic structure of future NFAs.

The lattice of β-ITIC-Th comprises a network of inter-penetrating molecules (Figure 6), where almost no π···π
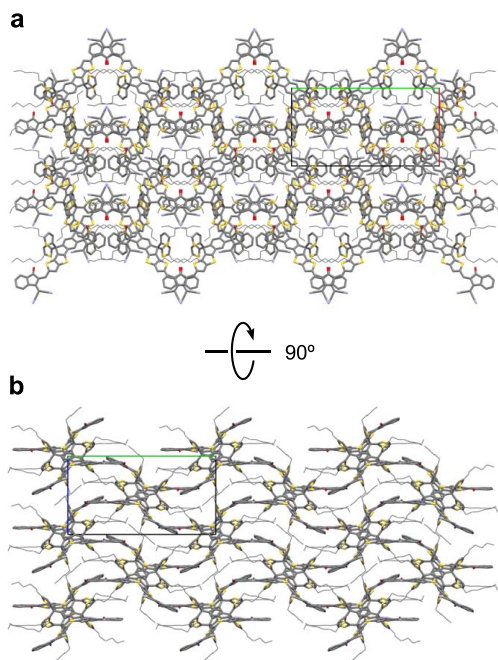

Figure 6. Lattice of ITIC-Th determined from MicroED. β-ITIC-Th MicroED structure viewed along the *c*-axis (a) and *a*-axis (b). Hydrogens are omitted for clarity, and alkyl chains are depicted as wireframe structures. The red, green, and blue axes correspond to the *a*, *b*, and *c* axes of the unit cell, respectively. The arrow represents a 90° rotation of the crystal around the given axis.

stacking is observed. The only contacts that could potentially be classified as π···π stacking are between one of the pendant thiophenes of the HC conformer and the phenyl ring of an IC group of the LC conformer (4.2 Å) and between pendant thiophene of the LC conformer and a methine group of the HC conformer (3.8 Å). Due to the lack of π···π stacking between β-ITIC-Th molecules, most short intermolecular contacts consist of interactions between hydrogens of the alkyl chains and carbonyl, nitrile, or sulfur groups. Intermolecular short contacts between the LC conformers (Figure S8) involve interactions between the IC nitrile group and a hydrogen on the hexyl chain of another LC conformer. Similarly, intermolecular short contacts between the HC β-ITIC-Th conformers (Figure S9) involve interactions between the malononitrile and methine groups and hydrogens of the pendant hexyl chains and thiophene rings. The HC and LC conformers are arranged diagonally relative to each other, with two general types of molecular contacts: end-to-end (Figure S10a) and overlapping (Figure S10b). In the case of the end-to-end contacts, the carbonyl and nitrile groups play an important role in forming short contacts with hydrogens of the IC phenyl rings and hexyl chains. Sulfur atoms play an important role in the intermolecular interactions between

overlapping LC and HC conformers due to a number of S···S and S···H short intermolecular contacts between the thienothiophene rings of the IDTT backbone and the pendant thiophenes.

A previous report of the ITIC-Th X-ray crystal structure (α-ITIC-Th) showed that the lattice is best described as a brickwork-type packing motif.[17] The β-ITIC-Th MicroED structure is a different polymorph, with significantly more distorted backbones and very little π···π stacking. Similar polymorphism has been observed in ITIC, with one report (α-ITIC)[14] of a brickwork lattice and another (β-ITIC)[12] of a complex interpenetrating network similar to β-ITIC-Th. However, the backbones of the β-ITIC polymorph are not as contorted as β-ITIC-Th. Molecular dynamics simulations suggest that π-conjugated backbones are typically substantially bent in the amorphous phase.[12,42] Yet, such distortion away from planarity is unusual in a crystal. To the best of our knowledge, the significant backbone distortion, as observed in the β-ITIC-Th polymorph, has not been reported before in OSC crystals without intramolecularly induced torsion.[46]

Hirshfeld Surface Analysis. The polymorphism observed for ITIC-Th suggests that these arrangements are likely more complex, particularly due to our observation of significantly distorted conjugated backbones in β-ITIC-Th. As such, the α-ITIC-Th, β-ITIC-Th, EH-IDTBR, and MicroED o-IDTBR structures were examined by Hirshfeld surface analysis[47] to quantify the influence of different intermolecular interactions.

The Hirshfeld surface (i.e., the isosurface at which the contribution of a molecule's electron cloud to that of the crystal exceeds the contributions of all other molecules)[47] is a powerful tool for understanding the confluence of different intermolecular interactions that give rise to a particular lattice arrangement. It can be used to analyze and visualize intermolecular interactions in crystals[48,49] but has so far been used only sparingly in the study of OSCs.[18,50,51]

Contributions to the Hirshfeld surface area for each atom pair (H, C, N, O, and S) were quantified for β-ITIC-Th (Figure S11), α-ITIC-Th (Figure S12), EH-IDTBR (Figure S13), and o-IDTBR (Figure S14). These contacts can be broken down into four general categories (Figure 7): H···H
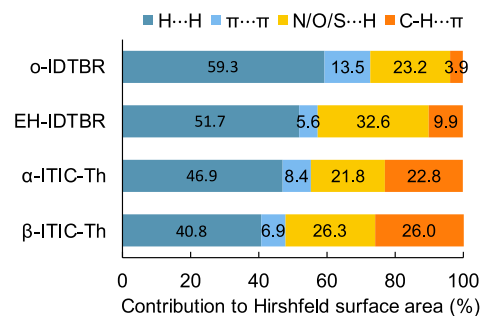

Figure 7. Comparison of Hirshfeld surface contributions for o-IDTBR, EH-IDTBR, α-ITIC-Th, and β-ITIC-Th. Comparison of four different types of interactions (H···H contacts, C−H···π interactions, π···π stacking, and N/O/S···H contacts) to the area of the Hirshfeld surface enables quantitative analysis of the contributions of intermolecular forces to the MicroED structures. The Hirshfeld surface analysis does not directly quantify C−H···π interactions or π···π stacking. H···C contacts were used to approximate the C−H···π interactions, and C···C, C···X (X = N, O, S), and X···X contacts were used to approximate the π···π stacking. Full details are given in the Methods section.

contacts, C−H⋯π interactions, π⋯π stacking, and intermolecular contacts between N, O, or S and H (N/O/S⋯H). The largest contribution to the surface area in both ITIC-Th atomic structures comes from H⋯H contacts (40.8% for β-ITIC-Th and 46.9% for α-ITIC-Th), which are largely due to interactions between the alkyl chains. The higher contribution from H⋯H contacts in the α-ITIC-Th X-ray crystal structure reflects their more efficient packing. C−H⋯π interactions also play an important role in both atomic structures: 26.0% for β-ITIC-Th and 22.8% for α-ITIC-Th. The lower contribution from C−H⋯π interactions in α-ITIC-Th reflects improved solid-state packing. Since C−H⋯π interactions are electronically undesirable compared to π⋯π stacking, these results suggest an improved intermolecular electronic coupling in α-ITIC-Th: areas of the π-conjugated backbone taken up by C−H⋯π interactions will not contribute as effectively to intermolecular electronic delocalization compared to the direct π-orbital overlap. As expected, an inverse relationship is observed for π⋯π stacking in the two ITIC-Th polymorphs. The contribution from π⋯π stacking in α-ITIC-Th is 8.4%, and 6.9% for β-ITIC-Th. The low degree of π⋯π stacking is surprising; however, it can be explained by the molecular design of NFAs, which limits contact between conjugated backbones to only the end acceptor units by creating steric hindrance around the donor core in the form of out-of-plane alkyl chains. Finally, N/O/S⋯H contacts play an important role in determining the conformational structure of ITIC-Th. In β-ITIC-Th, the contributions from N/O/S⋯H contacts are higher (26.3%) than those in α-ITIC-Th (21.8%). Analysis of the decomposed fingerprint plots of β-ITIC-Th (Figure S11) and α-ITIC-Th (Figure S12) provides further insight into the effects of different interactions on the atomic structure. The most notable differences between specific N/O/S⋯H contacts are observed for S⋯H and O⋯H interactions. In β-ITIC-Th, S⋯H contacts contribute to 11.4% of the Hirshfeld surface area. In α-ITIC-Th, S⋯H contacts only contribute to 7.1% of the surface area. Furthermore, the S⋯H contacts in β-ITIC-Th are much closer (∼2.5 Å) than in α-ITIC-Th (∼3.1 Å). The contribution to the Hirshfeld surface area from O⋯H contacts is lower in α-ITIC-Th (2.5%) than in β-ITIC-Th (3.5%). These observations are consistent with the analyses in the previous section. Since the majority of H⋯H contacts are due to interactions with the alkyl chains, these analyses suggest that solid-state packing arrangements that disfavor alkyl chain−donor core and alkyl chain−carbonyl contacts will lead to solid-state structures favoring more improved charge transport.

The two structures determined by MicroED are at opposite ends of the spectrum of NFA lattice topologies: β-ITIC-Th and o-IDTBR form a 0D lattice topology and a 3D wire mesh, respectively. The trends observed for the previous comparison of α-ITIC-Th and β-ITIC-Th apply in the case of o-IDTBR as well (Figure 7). The molecular structure and lattice topology of o-IDTBR are very different from those of the ITIC-Th atomic structures. Hirshfeld surface analysis of the EH-IDTBR X-ray crystal structure[17] serves to deconvolute the contributions from differences in molecular structure and lattice topology. The molecular structure of EH-IDTBR only differs from o-IDTBR by the topology of its side chains: 2-ethylhexl in EH-IDTBR and octyl in o-IDTBR. On the other hand, the slip-stacked lattice topology of EH-IDTBR is similar to that of α-ITIC-Th. The primary difference between the EH-IDTBR and α-ITIC-Th slip-stacked lattices is attributed to improved segregation of the side chains and backbones. This may arise

from the greater flexibility of the alkyl chains of EH-IDTBR compared to the 5-hexylthiophenyl chains of ITIC-Th. N/O/S⋯H contacts (32.6% of the Hirshfeld surface area) are larger in EH-IDTBR than in α-ITIC-Th because the EH-IDTBR molecules can form coplanar pairs with an EH-IDTBR molecule from another slip-stacked column. The smaller contribution from π⋯π stacking (5.6% of the Hirshfeld surface area) is explained by the different acceptor end groups of the ITIC-Th and IDTBR-type backbones. The planar IC end groups in the α-ITIC-Th molecule favor π⋯π stacking compared to the ethyl-rhodanine end groups of EH-IDTBR, where π⋯π stacking is only possible on one face of the backbone. The contributions of π⋯π stacking (13.5%) and N/O/S⋯H contacts (23.2%) to the Hirshfeld surface area in the o-IDTBR lattice are consistent with the trends observed in the different ITIC-Th polymorphs. H⋯H contacts constitute 51.7% of the Hirshfeld surface area of the EH-IDTBR lattice, and 59.3% of the surface area of the o-IDTBR lattice. Segregation of the alkyl chains from the backbones also explains the much lower contribution of C−H⋯π contacts to the Hirshfeld surface areas of both IDTBR-type lattices: 9.9% for EH-IDTBR and 3.9% for o-IDTBR. The larger contribution in EH-IDTBR compared to o-IDTBR is therefore due to differences between the slip-stacked and 3D wire mesh lattice topologies.

Computational Electronic Structure Calculations. Next, we perform first-principles quantum chemical simulations to elucidate the relationships between the previously discussed structures, their electronic properties, and charge carrier transport. Our modeling methodology is described in the Methods section, as well as in the Supporting Information.

As mentioned previously, the contorted backbones of the ITIC-Th MicroED structure, β-ITIC-Th, are unusual for crystals of π-conjugated materials. To better understand whether this polymorph could be technologically relevant, we calculated the absolute binding energy per molecule ($E_{binding}^{absolute}$) at the dispersion-corrected DFT level of theory (without vibrational and configurational energy) and compared these results to calculated values of other known NFA X-ray crystal structures (Table S3). The binding energy corresponds to a combination of the attractive and repulsive forces within the crystal, as well as the intramolecular conformational penalty, and represents the totality of the forces holding the atomic structure together. A greater $E_{binding}^{absolute}$ corresponds to a more stable polymorph. $E_{binding}^{absolute}$ was calculated to be 5.70 eV/mol for α-ITIC-Th, and 5.37 eV/mol for β-ITIC-Th. Although the binding energy of β-ITIC-Th is lower than that of α-ITIC-Th, its magnitude is within the range of $E_{binding}^{absolute}$ of similar NFAs (Figure S7) for which crystallographic data is available, such as β-ITIC (5.38 eV/mol),[12] ITIC-2Cl-β (4.63 eV/mol),[16] and a-ITIC-2Cl (4.86 eV/mol).[16] These results indicate that α-ITIC-Th is the slightly more stable polymorph of the two, confirming the feasibility of the β-ITIC-Th structure, and aligns well with the increases in π⋯π and alkyl−alkyl contacts detailed in the previous section. It is possible that MicroED permits the structure determination of crystals that would not normally be observed by traditional X-ray crystallography techniques. However, the origin of such a phenomenon remains unclear.

Electronic structure calculations of NFA lattices can be used to understand the impact of structure−property relationships relevant for future molecular design. In OPVs, charge transport

occurs in the hopping regime: charges migrate incoherently between different electronic sites.[52] If all sites are similar, the charge carrier mobility is the product of two factors. The squared hopping amplitude, η^2, strongly depends on intermolecular packing, particularly $\pi\cdots\pi$ stacking. The second factor (described more thoroughly in eq S3 in the Supporting Information) depends primarily on temperature and intramolecular properties. The hopping amplitude is easy to evaluate computationally, whereas the second factor is approximately the same for crystals of similar molecules such as those considered here. This allows us to relate packing to expected charge carrier mobility. For a pair of sites, the hopping amplitude is the product of the electronic coupling between them (charge transfer integral, t) and the hopping distance (a). Essentially, larger intermolecular electronic couplings and charge carrier hopping distances result in greater charge carrier mobility. For a crystal (lattice of sites), the hopping amplitude, η, along a given crystallographic direction properly summates over hops between all possible pairs of sites. DFT calculations were carried out for the optimal geometries of our MicroED structures and X-ray crystal structures of NFAs reported in the literature (Table 1). We initially consider pairwise couplings and hopping amplitudes, followed by a discussion of charge transport in the entire crystal.

The NFAs that form 3D wire mesh lattices display the best pairwise intermolecular electronic couplings (Table 1). In the case of o-IDTBR, there are three nonequivalent contacts with different transfer integral values. Electronic structure simulations show that the difference in onsite energies induced by the local environment (intramolecular L−R symmetry broken by crystallographic symmetry) is approximately 50 meV for o-IDTBR (Table S5), which decreases charge carrier mobility compared to the fully symmetric case. The magnitudes of the intermolecular couplings for RR and LR/RL contacts are similar (118 and 114 meV, respectively), while its amplitude for LL is approximately four times weaker (30 meV). Consequently, the η^2 value for LL contacts (0.012 eV$^2\cdot$Å^2) is only 3−5% of the other two. Overall, the wire mesh topology of the o-IDTBR atomic structure enables good electronic delocalization throughout the crystal. However, the small η^2 of the LL contact is a potential point of failure. This is likely due to the sensitivity of t to intermolecular geometry (e.g., a mismatch of the orbital phases as a result of relative shifts in the longitudinal direction of the two o-IDTBR molecules) and intermolecular contact area, as previously discussed for p-DTS(FBTTh$_2$)$_2$ and other molecules.[53,54]

a-ITIC-2Cl forms a 3D wire mesh lattice similar to that of o-IDTBR. However, the contacts between molecules are more complex since there are two symmetry-nonequivalent molecules with six different contacts (Figure S17). Some of the intermolecular electronic couplings are stronger than those in the o-IDTBR crystal: 177 and 139 meV for the R′R′ and RR′ contacts, respectively (Table 1). However, there is a substantial difference in the onsite energies of the two terminal electron-acceptor groups: the chlorinated end is 0.13 eV lower in energy compared to the nonchlorinated end. Thus, charge transport through this lattice is expected to suffer as a result of the differences in onsite energies.

Y6 (Figure S7f) also forms a 3D wire mesh lattice.[18] However, the contacts in the Y6 lattice are much better ($t = 101−160$ meV) compared to o-IDTBR and a-ITIC-2Cl, likely due to the crescent shape of the molecule, which results in an

Table 1. Intermolecular Electronic Couplings in a Number of NFA Lattices[a]

monomer	mul.	t (meV)	a (Å)	η^2 (eV$^2\cdot$Å^2)	contact
		o-IDTBR (MicroED)			
4 0$\bar{1}$1	4	118	5	0.359	RR
2 001	8	114	4	0.250	LR/RL
4 100	4	30	4	0.012	LL
		a-ITIC-2Cl[16]			
4′ $\bar{1}$11	2	177	9	2.746	R′R′
2 00$\bar{1}$	4	139	8	1.113	RR′
2 000	4	110	6	0.443	LL′
3 11$\bar{1}$	2	103	4	0.160	RR
4′ 000	2	91	4	0.140	L′L′
3 000	2	60	4	0.073	LL
		Y6[18]			
8 00$\bar{1}$	8	112	9	1.113	RR
2 100	8	160	4	0.303	RR
2 000	8	149	4	0.291	LL
4 00$\bar{1}$	8	101	4	0.150	LL
		EH-IDTBR[17]			
1 011	2	110	4	0.166	
1 001	2	35	11	0.137	
		ITIC-2Cl-β[16]			
2 000	4	55	5	0.066	
2 100	4	14	4	0.003	
		β-ITIC-Th (MicroED)			
4 1$\bar{1}$1	8	4	29	0.013	
2 000	8	6	8	0.002	
		α-ITIC-Th[17]			
1 01$\bar{1}$	2	72	5	0.122	
		β-ITIC[12]			
2 000	4	25	8	0.038	

[a]Calculated intermolecular electronic couplings (t), site-to-site hopping distances (a), and hopping amplitudes (η^2) of various NFA crystals. The monomer code "m ijk" refers to molecule m translated by i, j, and k unit cells along the first, second, and third translation vectors, respectively. The coupling is given between the "1 000" monomer and the listed monomer unless a prime is present, denoting the second symmetry-nonequivalent molecule (2 000). Only symmetry-nonequivalent dimers are listed, and their multiplicity per unit cell is given in the mul. column. There are two electronic sites per molecule. Transfer integrals and intramolecular electronic couplings calculated for the experimental geometry are also listed in Table S4. The last column provides the contact type according to Figures 3 and S17 for cases of multiple contact types.

increased intermolecular contact area and tolerance to thermal fluctuations. Unlike o-IDTBR and a-ITIC-2Cl, the Y6 lattice does not suffer from uneven contact problems (Table 1), leading to more balanced η^2 values (ranging from 0.150 to 1.113 eV$^2\cdot$Å^2). The strong intermolecular electronic couplings and more uniform contacts in the Y6 crystal rationalize the sudden rise to prominence of Y6 and its derivatives.[9,10,18]

EH-IDTBR (Figure S7g), which forms a slip-stacked lattice, only differs in the molecular structure from o-IDTBR by the topology of its alkyl chains. However, their lattice arrangements are very different. The reported X-ray crystal structure of EH-IDTBR is a lattice formed by slip-stacked backbones, where charges can only move along a 2D conjugated backbone network.[17] Our calculations reveal that there are uneven intermolecular electronic couplings between the two ends of the EH-IDTBR molecule (Table 1), where one contact is approximately three times smaller (35 meV) because of an

Table 2. Charge-Transport Descriptors for a Number of NFA Lattices[a]

crystal	η_1 (eV·Å)	η_2 (eV·Å)	η_3 (eV·Å)	bandspan (eV)	bandwidth (eV)	lattice type	connectivity
Y6[18]	0.99	0.92	0.39	0.88	0.26	wire mesh	3D
o-IDTBR	1.04	0.35	0.19	0.65	0.19	wire mesh	3D
EH-IDTBR[17]	1.32	0.22	0.03	0.55	0.17	slipped stack	1D-2D
α-ITIC-Th[17]	0.94	0.08	0.00	0.53	0.19	slipped stack	1D
ITIC-2Cl-β[16]	0.74	0.07	0.00	0.46	0.17	broken mesh	1D

[a]Hopping amplitude (η_{1-3}), bandspan, and bandwidth are considered electronic descriptors of charge carrier mobility. NFA lattices with 3D connectivity are found to have superior charge carrier mobility descriptors.

inferior interaction (not $\pi\cdots\pi$ stacking). However, the η^2 for both contacts are equivalent due to the increased a in the weaker contact.

The ITIC-2Cl-β crystal lattice[16] is topologically similar to that of EH-IDTBR. However, there are two symmetry inequivalent molecules in the crystal. In comparison to o-IDTBR, this can be considered a "broken wire mesh" lattice, where the acceptor groups of the molecules fail to establish a connection in the third dimension. Intermolecular couplings (55 and 14 meV) are similar in magnitude to the smallest coupling in EH-IDBTR and result in very small η^2 values of 0.066 and 0.003 eV^2·Å^2, respectively (Table 1).

As discussed above, β-ITIC-Th has a significantly different lattice arrangement. As a result of the lack of $\pi\cdots\pi$ stacking in the crystal, calculations predict poor electron transport. The calculated η^2 values (0.013 and 0.002 eV^2·Å^2, Table 1) are at the limit of the accuracy of rigid-geometry calculations since thermal fluctuations of η^2 are usually larger than 0.01 eV^2·Å^2. Since the calculated intermolecular electronic couplings in the β-ITIC-Th structure are smaller than 10 meV, charge transport is likely fluctuation-driven. Charge carriers can only move as a result of thermal fluctuations of the atomic structure that facilitate a given charge transfer event, as is typically observed in biopolymers such as the pili of *Geobacter sulfurreducens*.[55]

Similar packing is observed in the X-ray crystal structure of β-ITIC, but the pairwise intermolecular electronic couplings suggest that it is a better material for charge transport (Table 1). This can likely be attributed to the differences in backbone torsion between the two molecules. However, their origins currently remain unclear since the only difference between ITIC and ITIC-Th is the nature of the pendant aromatic rings: phenyl in ITIC and thiophenyl in ITIC-Th.

α-ITIC-Th exhibits much better electron transport properties than its newly discovered polymorph, β-ITIC-Th. The α-ITIC-Th X-ray crystal structure[17] forms a slip-stacked lattice similar to EH-IDTBR. However, there is only one type of contact due to differences in the overlap extent and torsion between heterocycles on each end of the molecule. It is noteworthy that ITIC-Th has achieved such success in OPV devices despite its inferior intermolecular electronic coupling in both polymorphs compared to that in o-IDTBR.[38] This may be attributable to distinct single-crystal and bulk heterojunction crystallite packing, which have previously been observed for OSCs.[43] During single-crystal growth, thermodynamics factors remain dominant, while kinetic factors are more important during thin film formation.[56,57]

To understand how molecular structure and lattice topology influence charge carrier mobility, we further calculate five relevant descriptors. The three hopping amplitudes (eigenvalues of the hopping amplitude tensor) characterize charge transport in the hopping regime. The other two quantities describe the electronic band structure: the bandspan is the

difference between the highest and lowest band energies and the root-mean-square bandwidth characterizes charge transport beyond the small polaron hopping approximation.[52] Larger values of these descriptors correspond to a larger expected charge carrier mobility. We note that mobility depends on a multitude of parameters, which are challenging to control experimentally or account for theoretically. However, the use of appropriate electronic descriptors isolates the influence of only one parameter: in this case, molecular geometry and packing.

Of all of the NFAs for which electronic structure descriptors were calculated, those that form a 3D wire mesh lattice generally have the largest values. Y6 and o-IDTBR should have the highest electron mobilities (Table 2), consistent with their success in OPV devices. Although o-IDTBR has the larger hopping amplitude ($\eta_1 = 1.04$ eV·Å), that of the Y6 lattice is more balanced (between 0.99 and 0.39 eV·Å). Furthermore, Y6 also has a larger bandspan (0.88 eV) and bandwidth (0.26 eV) than o-IDTBR. These descriptors for the Y6 lattice are close to those of well-known high-performing OSC crystals such as F$_2$-TCNQ,[58] hexacene,[59] and TIPS-pentacene[60] (Table S6).

NFAs that do not form a wire mesh lattice should have lower charge carrier mobilities due to their poorer mobility descriptors. The NFAs with 1D lattice connectivity have one large η, while the others are much smaller (Table 2). This reflects the lower degree of connections for charge transport through the lattice. The band structure descriptors (bandspan and bandwidth) of EH-IDTBR, α-ITIC-Th, and ITIC-2Cl-β are similar to those of the well-known molecular donors (Table S6): p-DTS(FBTTh$_2$)$_2$, which forms a slip-stacked lattice,[53] as well as p-DTS(PTTh$_2$)$_2$, which forms a 1D π-stacked lattice.[23]

Of all the lattices examined herein, the wire mesh topology is the only one with 3D connectivity. Among the four considered wire mesh crystals, o-IDTBR and Y6 are the best electron transport materials: ITIC-2Cl-β has broken contacts, and a-ITIC-2Cl has a substantial energy penalty for intramolecular electron transfer due to the asymmetry of the acceptor groups. Nevertheless, one contact in o-IDTBR is four times smaller than the other three, resulting in imperfect 3D connectivity.

Extended side chains in most if not all large oligomers are intrinsically disordered with a multitude of nearly isoenergetic conformations similar to what has been previously observed in P3HT.[43] However, the presence of extended side chains may be critical for obtaining a desirable morphology in an OSC device. On the other hand, in most cases (except o-IDTBR, a-ITIC-2Cl, and Y6), the side chains severely block charge carrier transport, reducing the dimension of the transport channel to quasi-one-dimensional or a percolating network. Interestingly, an estimated (via hopping amplitudes) charge-transport efficiency for crystals correlates well with measured mobility in thin films. This implies that intermolecular packing

in thin films correlates with packing in crystals, thus dramatically simplifying the computational design of such materials.

CONCLUSIONS

The 3D wire mesh lattice topology has been previously suspected to be responsible for the increase in performance of the new generation of NFAs, as well as underpin their superiority to fullerenes as electron-acceptor materials in organic photovoltaics. However, molecular design principles toward optimal self-assembly into the desired crystal lattice are yet to be developed. Our MicroED structural determinations and results of electronic structure calculations convey a number of important lessons. In particular, the 3D wire mesh crystal lattice potentially offers the best network for robust charge transport in multiple dimensions. Unfortunately, many of the currently known NFAs that organize into such a lattice suffer from uneven electronic couplings at the wire mesh nodes, which are potential bottlenecks for charge transport. Y6 does not have this problem, which may partly explain its success. To make charge transport in NFA crystals more robust, future designs will need to take into account the possibility of uneven contacts due to either undesirable backbone overlaps or asymmetric chemical structures. Analysis of the intermolecular contacts suggests that promoting the segregation of alkyl chains and aromatic backbones, and favoring face-to-face stacking of the conjugated backbones, would facilitate the desirable 3D wire mesh lattice. In theory, better topologies are possible since this space is largely unexplored. It should be noted that the performance of NFAs in real active layers is not solely dictated by the lattice of the crystallites in the thin film. There are many additional morphological factors such as degree of crystallinity, packing in the amorphous phase, intercrystallite charge transport, and charge-transport percolation that affect a material's performance in a real device. The introduction of one or more additional materials in a bulk heterojunction blend may affect these morphological features, as well as the lattice organization of the NFA, as a result of different processing conditions and intermolecular interactions. However, these changes must be determined experimentally because predicting the morphology of bulk heterojunctions is still extremely challenging.

Further complications in designing future NFAs arise from challenges in structure determination and the possibility of polymorphism. In this study, MicroED discovered a new polymorph of ITIC-Th that has the most distorted NFA backbone ever reported. This experimental approach has the potential to become an important tool for understanding the relationships between crystallization or processing conditions and OSC solid-state structure. Identifying the atomic structure of o-IDTBR from a sample of a commercially available powder demonstrates its potential to open up materials and chemical space for crystallographic study. Thus, MicroED can enable researchers to more easily determine the atomic structure of OSCs by allowing them to study crystals that are too small for single-crystal X-ray crystallography and without going through the laborious crystal growth pipelines required for the latter.

METHODS

Sample Preparation. Samples of o-IDTBR and ITIC-Th were purchased from 1-Material Inc. o-IDTBR was used without further purification. ITIC-Th microcrystals were prepared by dissolving the material in chlorobenzene and subsequent vapor diffusion with

hexanes as the antisolvent at 2−3 °C, resulting in a suspension of microcrystals. The mother liquor was removed, and the microcrystals were dried overnight under vacuum. Both materials were stored in sealed glass vials prior to use.

Preclipped Quantifoil Cu300 mesh grids (R2/2, o-IDTBR; R1.2/1.3, ITIC-Th) were added to either vial and shaken gently to apply the sample to the grids. The grids were extracted from the vials using forceps, and then lightly tapped to remove excess material.

Grids were dipped directly into liquid nitrogen, placed in the sample cassette, and loaded into a Thermo-Fisher Talos Arctica transmission electron cryomicroscope.

Data Collection and Processing. MicroED data collection was performed as previously described.[33,61] Briefly, the astigmatism of the lenses, beam alignment, and the grid's sample z height were adjusted prior to data collection. The microscope was operated at an acceleration voltage of 200 kV at liquid nitrogen temperatures (~80 K). Crystals were identified in overfocused diffraction mode. Identified crystals were then centered in a near-parallel electron beam using an exposure of ~0.01 e⁻ Å⁻² s⁻¹. Data were collected in the rolling shutter mode on a complementary metal oxide-semiconductor-based CetaD 4k × 4k camera with pixels binned by 2. Samples were rotated continuously in the electron beam at a rate of ~0.1−0.3° s⁻¹ for ~30−60°. Frames were read out every 3 s while the crystal was rotated.

The diffraction movies were originally saved in the MRC format and converted to the SMV format using in-house software, which is freely available online (https://cryoem.ucla.edu/pages/MicroED), and processed as described.[62]

Once the frames had been converted, XDS, XDSCONV, and SHELX were used to index and integrate, convert to the SHELX format, and scale and merge, respectively.[63,64] Both structures were solved by direct methods using the small molecule solution program SHELXT and refined with riding hydrogens in SHELXL using electron scattering factors as described.[65,66] However, the long, floppy hydrocarbon chains were refined with distance restraints, whereas the rest of the atoms in the backbones were unrestrained.

Computational Methodology. Hirshfeld surfaces were generated using the experimentally determined atomic structure coordinates, and all electron density calculations were performed using the default methods in CrystalExplorer 17.5.[67] H···H contacts were determined from the H···H contribution to the surface area. H···C contributions to the surface area were used as a proxy for C−H···π interactions. The sum of all C···C, C···X (where X = N, O, or S), and X···X contributions to the surface area were used as a proxy for π···π stacking. N/O/S···H contacts were determined from the sum of all H···X contributions to the surface area. Due to the static disorder of the 2-ethylhexyl side chains in EH-IDTBR X-ray crystal structure, a single conformation of the side chains was chosen for Hirshfeld surface calculations.

All DFT calculations were performed using the Gaussian 16[68] and VASP 5.4[69] commercial packages. For molecules and their clusters, we used the CAM-B3LYP/6-31G* method (with D3 empirical corrections whenever appropriate), which has been thoroughly benchmarked in our recent works.[41,43] For crystals we used the PBE functional with D3 empirical corrections and PAW pseudopotentials with at least a 400 eV plane-wave cutoff (abbreviated as PBE-D3/PAW400). The coarse-grained Hamiltonian for holes was calculated using a well-established methodology.[52] In the case of electrons, a minimal reasonable model includes two sites per molecule, and thus, we used a more sophisticated approach introduced in ref 70. A detailed description of the computational methodology is given in the Supporting Information.

ASSOCIATED CONTENT

ⓢ Supporting Information

The Supporting Information is available free of charge at https://pubs.acs.org/doi/10.1021/acs.chemmater.0c04111.

Analysis of the o-IDTBR MicroED structure, analysis of the ITIC-Th MicroED structure, Hirshfeld surface

analysis; computational methodology, calculated structural properties, and calculated electronics properties (PDF)

■ AUTHOR INFORMATION

Corresponding Authors

Andriy Zhugayevych − *Skolkovo Institute of Science and Technology, 143026 Moscow, Russia;* ◉ orcid.org/0000-0003-4713-1289; Email: A.Zhugayevych@skoltech.ru

Tamir Gonen − *Howard Hughes Medical Institute, David Geffen School of Medicine, Departments of Biological Chemistry and Physiology, University of California, Los Angeles, California 90095, United States;* ◉ orcid.org/0000-0002-9254-4069; Email: tgonen@g.ucla.edu

Martin Seifrid − *Center for Polymers and Organic Solids, Department of Chemistry and Biochemistry, University of California, Santa Barbara, California 93106, United States;* ◉ orcid.org/0000-0001-5238-0058; Email: mseifrid@ucsb.edu

Authors

Steve Halaby − *Howard Hughes Medical Institute, David Geffen School of Medicine, Departments of Biological Chemistry and Physiology, University of California, Los Angeles, California 90095, United States*

Michael W. Martynowycz − *Howard Hughes Medical Institute, David Geffen School of Medicine, Departments of Biological Chemistry and Physiology, University of California, Los Angeles, California 90095, United States*

Ziyue Zhu − *Center for Polymers and Organic Solids, Department of Chemistry and Biochemistry, University of California, Santa Barbara, California 93106, United States*

Sergei Tretiak − *Physics and Chemistry of Materials, Theoretical Division and Center for Integrated Nanotechnologies, Los Alamos National Laboratory, Los Alamos, New Mexico 87545, United States; Skolkovo Institute of Science and Technology, 143026 Moscow, Russia;* ◉ orcid.org/0000-0001-5547-3647

Complete contact information is available at:
https://pubs.acs.org/10.1021/acs.chemmater.0c04111

Author Contributions

M.S., T.G., A.Z., and S.T. conceived and managed the project. M.S. and Z.Z. grew the single crystals. S.H. collected the MicroED data. S.H., M.W.M., and M.S. analyzed the MicroED data. M.S. performed the Hirshfeld surface calculations. A.Z. performed the DFT calculations. S.H., S.T., A.Z., T.G., and M.S. contributed to writing the paper. All authors commented on the manuscript.

Notes

The authors declare no competing financial interest.
The data supporting the results of this work are available from the authors upon reasonable request. The structure factors and coordinates for the o-IDTBR (2033974) and ITIC-Th (2033973) structures have been deposited in the CCDC.

■ REFERENCES

(1) *The WSPC Reference on Organic Electronics: Organic Semiconductors: Volume 2: Fundamental Aspects of Materials and Applications*; Marder, S. R.; Bredas, J.-L., Eds.; World Scientific Publishing Co. Pte. Ltd.: Singapore, 2016.

(2) Coughlin, J. E.; Henson, Z. B.; Welch, G. C.; Bazan, G. C. Design and Synthesis of Molecular Donors for Solution-Processed High-Efficiency Organic Solar Cells. *Acc. Chem. Res.* **2014**, *47*, 257−270.

(3) Li, Y. Molecular Design of Photovoltaic Materials for Polymer Solar Cells: Toward Suitable Electronic Energy Levels and Broad Absorption. *Acc. Chem. Res.* **2012**, *45*, 723−733.

(4) Seifrid, M.; Reddy, G. N. M.; Chmelka, B. F.; Bazan, G. C. Insight into the Structures and Dynamics of Organic Semiconductors through Solid-State NMR Spectroscopy. *Nat. Rev. Mater.* **2020**, *5*, 910−930.

(5) Lin, Y.; Li, Y.; Zhan, X. Small Molecule Semiconductors for High-Efficiency Organic Photovoltaics. *Chem. Soc. Rev.* **2012**, *41*, 4245.

(6) Facchetti, A. π-Conjugated Polymers for Organic Electronics and Photovoltaic Cell Applications. *Chem. Mater.* **2011**, *23*, 733−758.

(7) Ganesamoorthy, R.; Sathiyan, G.; Sakthivel, P. Review: Fullerene Based Acceptors for Efficient Bulk Heterojunction Organic Solar Cell Applications. *Sol. Energy Mater. Sol. Cells* **2017**, *161*, 102−148.

(8) Green, M. A.; Dunlop, E. D.; Levi, D. H.; Hohl-Ebinger, J.; Yoshita, M.; Ho-Baillie, A. W. Y. Solar Cell Efficiency Tables (Version 54). *Prog. Photovolt. Res. Appl.* **2019**, *27*, 565−575.

(9) Liu, Q.; Jiang, Y.; Jin, K.; Qin, J.; Xu, J.; Li, W.; Xiong, J.; Liu, J.; Xiao, Z.; Sun, K.; Yang, S.; Zhang, X.; Ding, L. 18% Efficiency Organic Solar Cells. *Sci. Bull.* **2020**, *65*, 272−275.

(10) Cui, Y.; Yao, H.; Zhang, J.; Xian, K.; Zhang, T.; Hong, L.; Wang, Y.; Xu, Y.; Ma, K.; An, C.; He, C.; Wei, Z.; Gao, F.; Hou, J. Single-Junction Organic Photovoltaic Cells with Approaching 18% Efficiency. *Adv. Mater.* **2020**, *32*, No. 1908205.

(11) Yan, C.; Barlow, S.; Wang, Z.; Yan, H.; Jen, A. K.-Y.; Marder, S. R.; Zhan, X. Non-Fullerene Acceptors for Organic Solar Cells. *Nat. Rev. Mater.* **2018**, *3*, No. 18003.

(12) Han, G.; Guo, Y.; Song, X.; Wang, Y.; Yi, Y. Terminal π−π Stacking Determines Three-Dimensional Molecular Packing and Isotropic Charge Transport in an A−π−A Electron Acceptor for Non-Fullerene Organic Solar Cells. *J. Mater. Chem. C* **2017**, *5*, 4852−4857.

(13) Shi, X.; Zuo, L.; Jo, S. B.; Gao, K.; Lin, F.; Liu, F.; Jen, A. K.-Y. Design of a Highly Crystalline Low-Band Gap Fused-Ring Electron Acceptor for High-Efficiency Solar Cells with Low Energy Loss. *Chem. Mater.* **2017**, *29*, 8369−8376.

(14) Aldrich, T. J.; Matta, M.; Zhu, W.; Swick, S. M.; Stern, C. L.; Schatz, G. C.; Facchetti, A.; Melkonyan, F. S.; Marks, T. J. Fluorination Effects on Indacenodithienothiophene Acceptor Packing and Electronic Structure, End-Group Redistribution, and Solar Cell Photovoltaic Response. *J. Am. Chem. Soc.* **2019**, *141*, 3274−3287.

(15) Qu, J.; Zhao, Q.; Zhou, J.; Lai, H.; Liu, T.; Li, D.; Chen, W.; Xie, Z.; He, F. Multiple Fused Ring-Based Near-Infrared Nonfullerene Acceptors with an Interpenetrated Charge-Transfer Network. *Chem. Mater.* **2019**, *31*, 1664−1671.

(16) Lai, H.; Chen, H.; Zhou, J.; Qu, J.; Wang, M.; Xie, W.; Xie, Z.; He, F. 3D Interpenetrating Network for High-Performance Non-

fullerene Acceptors via Asymmetric Chlorine Substitution. *J. Phys. Chem. Lett.* **2019**, *10*, 4737−4743.

(17) Bristow, H.; Thorley, K. J.; White, A. J. P.; Wadsworth, A.; Babics, M.; Hamid, Z.; Zhang, W.; Paterson, A. F.; Kosco, J.; Panidi, J.; Anthopoulos, T. D.; McCulloch, I. Impact of Nonfullerene Acceptor Side Chain Variation on Transistor Mobility. *Adv. Electron. Mater.* **2019**, *5*, No. 1900344.

(18) Zhu, L.; Zhang, M.; Zhou, G.; Hao, T.; Xu, J.; Wang, J.; Qiu, C.; Prine, N.; Ali, J.; Feng, W.; Gu, X.; Ma, Z.; Tang, Z.; Zhu, H.; Ying, L.; Zhang, Y.; Liu, F. Efficient Organic Solar Cell with 16.88% Efficiency Enabled by Refined Acceptor Crystallization and Morphology with Improved Charge Transfer and Transport Properties. *Adv. Energy Mater.* **2020**, *10*, No. 1904234.

(19) Dai, S.; Zhou, J.; Chandrabose, S.; Shi, Y.; Han, G.; Chen, K.; Xin, J.; Liu, K.; Chen, Z.; Xie, Z.; Ma, W.; Yi, Y.; Jiang, L.; Hodgkiss, J. M.; Zhan, X. High-Performance Fluorinated Fused-Ring Electron Acceptor with 3D Stacking and Exciton/Charge Transport. *Adv. Mater.* **2020**, *32*, No. 2000645.

(20) Zhu, W.; Spencer, A. P.; Mukherjee, S.; Alzola, J. M.; Sangwan, V. K.; Amsterdam, S. H.; Swick, S. M.; Jones, L. O.; Heiber, M. C.; Herzing, A. A.; Li, G.; Stern, C. L.; DeLongchamp, D. M.; Kohlstedt, K. L.; Hersam, M. C.; Schatz, G. C.; Wasielewski, M. R.; Chen, L. X.; Facchetti, A.; Marks, T. J. Crystallography, Morphology, Electronic Structure, and Transport in Non-Fullerene/Non-Indacenodithieno-thiophene Polymer:Y6 Solar Cells. *J. Am. Chem. Soc.* **2020**, *142*, 14532−14547.

(21) Zhang, G.; Chen, X.-K.; Xiao, J.; Chow, P. C. Y.; Ren, M.; Kupgan, G.; Jiao, X.; Chan, C. C. S.; Du, X.; Xia, R.; Chen, Z.; Yuan, J.; Zhang, Y.; Zhang, S.; Liu, Y.; Zou, Y.; Yan, H.; Wong, K. S.; Coropceanu, V.; Li, N.; Brabec, C. J.; Bredas, J.-L.; Yip, H.-L.; Cao, Y. Delocalization of Exciton and Electron Wavefunction in Non-Fullerene Acceptor Molecules Enables Efficient Organic Solar Cells. *Nat. Commun.* **2020**, *11*, No. 3943.

(22) Coropceanu, V.; Li, H.; Winget, P.; Zhu, L.; Brédas, J.-L. Electronic-Structure Theory of Organic Semiconductors: Charge-Transport Parameters and Metal/Organic Interfaces. *Annu. Rev. Mater. Res.* **2013**, *43*, 63−87.

(23) Zhugayevych, A.; Postupna, O.; Bakus, R. C., II; Welch, G. C.; Bazan, G. C.; Tretiak, S. Ab Initio Study of a Molecular Crystal for Photovoltaics: Light Absorption, Exciton and Charge Carrier Transport. *J. Phys. Chem. C* **2013**, *117*, 4920−4930.

(24) Nannenga, B. L.; Shi, D.; Leslie, A. G. W.; Gonen, T. High-Resolution Structure Determination by Continuous-Rotation Data Collection in MicroED. *Nat. Methods* **2014**, *11*, 927−930.

(25) Nannenga, B. L.; Bu, G.; Shi, D. The Evolution and the Advantages of MicroED. *Front. Mol. Biosci.* **2018**, *5*, No. 114.

(26) Martynowycz, M. W.; Gonen, T. From Electron Crystallography of 2D Crystals to MicroED of 3D Crystals. *Curr. Opin. Colloid Interface Sci.* **2018**, *34*, 9−16.

(27) Rodriguez, J. A.; Ivanova, M. I.; Sawaya, M. R.; Cascio, D.; Reyes, F. E.; Shi, D.; Sangwan, S.; Guenther, E. L.; Johnson, L. M.; Zhang, M.; Jiang, L.; Arbing, M. A.; Nannenga, B. L.; Hattne, J.; Whitelegge, J.; Brewster, A. S.; Messerschmidt, M.; Boutet, S.; Sauter, N. K.; Gonen, T.; Eisenberg, D. S. Structure of the Toxic Core of α-Synuclein from Invisible Crystals. *Nature* **2015**, *525*, 486−490.

(28) Nannenga, B. L.; Shi, D.; Hattne, J.; Reyes, F. E.; Gonen, T. Structure of Catalase Determined by MicroED. *eLife* **2014**, *3*, No. e03600.

(29) Liu, S.; Gonen, T. MicroED Structure of the NaK Ion Channel Reveals a Na + Partition Process into the Selectivity Filter. *Commun. Biol.* **2018**, *1*, 38.

(30) Xu, H.; Lebrette, H.; Yang, T.; Srinivas, V.; Hovmöller, S.; Högbom, M.; Zou, X. A Rare Lysozyme Crystal Form Solved Using Highly Redundant Multiple Electron Diffraction Datasets from Micron-Sized Crystals. *Structure* **2018**, *26*, 667−675.e3.

(31) Xu, H.; Lebrette, H.; Clabbers, M. T. B.; Zhao, J.; Griese, J. J.; Zou, X.; Högbom, M. Solving a New R2lox Protein Structure by Microcrystal Electron Diffraction. *Sci. Adv.* **2019**, *5*, No. eaax4621.

(32) Zhou, H.; Luo, F.; Luo, Z.; Li, D.; Liu, C.; Li, X. Programming Conventional Electron Microscopes for Solving Ultrahigh-Resolution Structures of Small and Macro-Molecules. *Anal. Chem.* **2019**, *91*, 10996−11003.

(33) Jones, C. G.; Martynowycz, M. W.; Hattne, J.; Fulton, T. J.; Stoltz, B. M.; Rodriguez, J. A.; Nelson, H. M.; Gonen, T. The CryoEM Method MicroED as a Powerful Tool for Small Molecule Structure Determination. *ACS Cent. Sci.* **2018**, *4*, 1587−1592.

(34) Das, P. P.; Mugnaioli, E.; Nicolopoulos, S.; Tossi, C.; Gemmi, M.; Galanis, A.; Borodi, G.; Pop, M. M. Crystal Structures of Two Important Pharmaceuticals Solved by 3D Precession Electron Diffraction Tomography. *Org. Process Res. Dev.* **2018**, *22*, 1365−1372.

(35) Panova, O.; Ophus, C.; Takacs, C. J.; Bustillo, K. C.; Balhorn, L.; Salleo, A.; Balsara, N.; Minor, A. M. Diffraction Imaging of Nanocrystalline Structures in Organic Semiconductor Molecular Thin Films. *Nat. Mater.* **2019**, *18*, 860−865.

(36) Levine, A. M.; Bu, G.; Biswas, S.; Tsai, E. H. R.; Braunschweig, A.; Nannenga, B. L. Crystal Structure and Orientation of Organic Semiconductor Thin Films by Microcrystal Electron Diffraction and Grazing-Incidence Wide-Angle X-Ray Scattering. *Chem. Commun.* **2020**, *56*, 4204−4207.

(37) Brinkmann, M. Insights in the Structural Complexity of Semi-Crystalline Polymer Semiconductors: Electron Diffraction Contributions. *Mater. Chem. Front.* **2020**, *4*, 1916−1929.

(38) Lin, Y.; Zhao, F.; He, Q.; Huo, L.; Wu, Y.; Parker, T. C.; Ma, W.; Sun, Y.; Wang, C.; Zhu, D.; Heeger, A. J.; Marder, S. R.; Zhan, X. High-Performance Electron Acceptor with Thienyl Side Chains for Organic Photovoltaics. *J. Am. Chem. Soc.* **2016**, *138*, 4955−4961.

(39) Holliday, S.; Ashraf, R. S.; Wadsworth, A.; Baran, D.; Yousaf, S. A.; Nielsen, C. B.; Tan, C.-H.; Dimitrov, S. D.; Shang, Z.; Gasparini, N.; Alamoudi, M.; Laquai, F.; Brabec, C. J.; Salleo, A.; Durrant, J. R.; McCulloch, I. High-Efficiency and Air-Stable P3HT-Based Polymer Solar Cells with a New Non-Fullerene Acceptor. *Nat. Commun.* **2016**, *7*, No. 11585.

(40) Baran, D.; Ashraf, R. S.; Hanifi, D. A.; Abdelsamie, M.; Gasparini, N.; Röhr, J. A.; Holliday, S.; Wadsworth, A.; Lockett, S.; Neophytou, M.; Emmott, C. J. M.; Nelson, J.; Brabec, C. J.; Amassian, A.; Salleo, A.; Kirchartz, T.; Durrant, J. R.; McCulloch, I. Reducing the Efficiency−Stability−Cost Gap of Organic Photovoltaics with Highly Efficient and Stable Small Molecule Acceptor Ternary Solar Cells. *Nat. Mater.* **2017**, *16*, 363−369.

(41) Tukachev, N. V.; Maslennikov, D. R.; Sosorev, A. Yu.; Tretiak, S.; Zhugayevych, A. Ground-State Geometry and Vibrations of Polyphenylenevinylene Oligomers. *J. Phys. Chem. Lett.* **2019**, *10*, 3232−3239.

(42) Kilina, S.; Dandu, N.; Batista, E. R.; Saxena, A.; Martin, R. L.; Smith, D. L.; Tretiak, S. Effect of Packing on Formation of Deep Carrier Traps in Amorphous Conjugated Polymers. *J. Phys. Chem. Lett.* **2013**, *4*, 1453−1459.

(43) Zhugayevych, A.; Mazaleva, O.; Naumov, A.; Tretiak, S. Lowest-Energy Crystalline Polymorphs of P3HT. *J. Phys. Chem. C* **2018**, *122*, 9141−9151.

(44) Zhou, C.; Cui, Q.; McDowell, C.; Seifrid, M.; Chen, X.; Brédas, J.-L.; Wang, M.; Huang, F.; Bazan, G. C. Topological Transformation of π-Conjugated Molecules Reduces Resistance to Crystallization. *Angew. Chem., Int. Ed.* **2017**, *56*, 9318−9321.

(45) Seifrid, M. T.; Reddy, G. N. M.; Zhou, C.; Chmelka, B. F.; Bazan, G. C. Direct Observation of the Relationship Between Molecular Topology and Bulk Morphology for a Pi-Conjugated Material. *J. Am. Chem. Soc.* **2019**, *141*, 5078−5082.

(46) Pascal, R. A. Twisted Acenes. *Chem. Rev.* **2006**, *106*, 4809−4819.

(47) Spackman, M. A.; Jayatilaka, D. Hirshfeld Surface Analysis. *CrystEngComm* **2009**, *11*, 19−32.

(48) Spackman, M. A.; McKinnon, J. J. Fingerprinting Intermolecular Interactions in Molecular Crystals. *CrystEngComm* **2002**, *4*, 378−392.

(49) McKinnon, J. J.; Jayatilaka, D.; Spackman, M. A. Towards Quantitative Analysis of Intermolecular Interactions with Hirshfeld Surfaces. *Chem. Commun.* **2007**, 3814−3816.

(50) Klues, M.; Witte, G. Crystalline Packing in Pentacene-like Organic Semiconductors. *CrystEngComm* **2018**, *20*, 63−74.

(51) Wang, C.; Hashizume, D.; Nakano, M.; Ogaki, T.; Takenaka, H.; Kawabata, K.; Takimiya, K. "Disrupt and Induce" Intermolecular Interactions to Rationally Design Organic Semiconductor Crystals: From Herringbone to Rubrene-like Pitched π-Stacking. *Chem. Sci.* **2020**, *11*, 1573−1580.

(52) Zhugayevych, A.; Tretiak, S. Theoretical Description of Structural and Electronic Properties of Organic Photovoltaic Materials. *Annu. Rev. Phys. Chem.* **2015**, *66*, 305−330.

(53) Cui, Q.; Hu, Y.; Zhou, C.; Teng, F.; Huang, J.; Zhugayevych, A.; Tretiak, S.; Nguyen, T.-Q.; Bazan, G. C. Single Crystal Microwires of P-DTS(FBTTh2)2 and Their Use in the Fabrication of Field-Effect Transistors and Photodetectors. *Adv. Funct. Mater.* **2018**, *28*, No. 1702073.

(54) Kwon, O.; Coropceanu, V.; Gruhn, N. E.; Durivage, J. C.; Laquindanum, J. G.; Katz, H. E.; Cornil, J.; Brédas, J. L. Characterization of the Molecular Parameters Determining Charge Transport in Anthradithiophene. *J. Chem. Phys.* **2004**, *120*, 8186−8194.

(55) Yan, H.; Chuang, C.; Zhugayevych, A.; Tretiak, S.; Dahlquist, F. W.; Bazan, G. C. Inter-Aromatic Distances in *Geobacter sulfurreducens* Pili Relevant to Biofilm Charge Transport. *Adv. Mater.* **2015**, *27*, 1908−1911.

(56) Hiszpanski, A. M.; Khlyabich, P. P.; Loo, Y.-L. Tuning Kinetic Competitions to Traverse the Rich Structural Space of Organic Semiconductor Thin Films. *MRS Commun.* **2015**, *5*, 407−421.

(57) Seifrid, M. T.; Oosterhout, S. D.; Toney, M. F.; Bazan, G. C. Kinetic Versus Thermodynamic Orientational Preferences for a Series of Isomorphic Molecular Semiconductors. *ACS Omega* **2018**, *3*, 10198−10204.

(58) Krupskaya, Y.; Gibertini, M.; Marzari, N.; Morpurgo, A. F. Band-Like Electron Transport with Record-High Mobility in the TCNQ Family. *Adv. Mater.* **2015**, *27*, 2453−2458.

(59) Watanabe, M.; Chang, Y. J.; Liu, S.-W.; Chao, T.-H.; Goto, K.; Islam, M. M.; Yuan, C.-H.; Tao, Y.-T.; Shinmyozu, T.; Chow, T. J. The Synthesis, Crystal Structure and Charge-Transport Properties of Hexacene. *Nat. Chem.* **2012**, *4*, 574−578.

(60) Anthony, J. E.; Brooks, J. S.; Eaton, D. L.; Parkin, S. R. Functionalized Pentacene: Improved Electronic Properties from Control of Solid-State Order. *J. Am. Chem. Soc.* **2001**, *123*, 9482−9483.

(61) Hattne, J.; Reyes, F. E.; Nannenga, B. L.; Shi, D.; de la Cruz, M. J.; Leslie, A. G. W.; Gonen, T. MicroED Data Collection and Processing. *Acta Crystallogr., Sect. A: Found. Adv.* **2015**, *71*, 353−360.

(62) Hattne, J.; Martynowycz, M. W.; Penczek, P. A.; Gonen, T. MicroED with the Falcon III Direct Electron Detector. *IUCrJ* **2019**, *6*, 921−926.

(63) Kabsch, W. XDS. *Acta Crystallogr., Sect. D: Biol. Crystallogr.* **2010**, *66*, 125−132.

(64) Kabsch, W. Integration, Scaling, Space-Group Assignment and Post-Refinement. *Acta Crystallogr., Sect. D: Biol. Crystallogr.* **2010**, *66*, 133−144.

(65) Sheldrick, G. M. SHELXT − Integrated Space-Group and Crystal-Structure Determination. *Acta Crystallogr., Sect. A: Found. Adv.* **2015**, *71*, 3−8.

(66) Sheldrick, G. M. Crystal Structure Refinement with SHELXL. *Acta Crystallogr., Sect. C: Struct. Chem.* **2015**, *71*, 3−8.

(67) Turner, M. J.; McKinnon, J. J.; Wolff, S. K.; Grimwood, D. J.; Spackman, P. R.; Jayatilaka, D.; Spackman, M. A. *CrystalExplorer 17.5*; University of Western Australia, 2017.

(68) Frisch, M. J.; Trucks, G. W.; Schlegel, H. B.; Scuseria, G. E.; Robb, M. A.; Cheeseman, J. R.; Scalmani, G.; Barone, V.; Petersson, G. A.; Nakatsuji, H.; Li, X.; Caricato, M.; Marenich, A. V.; Bloino, J.; Janesko, B. G.; Gomperts, R.; Mennucci, B.; Hratchian, H. P.; Ortiz, J. V.; Izmaylov, A. F.; Sonnenberg, J. L.; Williams; Ding, F.; Lipparini, F.; Egidi, F.; Goings, J.; Peng, B.; Petrone, A.; Henderson, T.; Ranasinghe, D.; Zakrzewski, V. G.; Gao, J.; Rega, N.; Zheng, G.; Liang, W.; Hada, M.; Ehara, M.; Toyota, K.; Fukuda, R.; Hasegawa, J.; Ishida, M.; Nakajima, T.; Honda, Y.; Kitao, O.; Nakai, H.; Vreven, T.; Throssell, K.; Montgomery, J. A., Jr.; Peralta, J. E.; Ogliaro, F.; Bearpark, M. J.; Heyd, J. J.; Brothers, E. N.; Kudin, K. N.; Staroverov, V. N.; Keith, T. A.; Kobayashi, R.; Normand, J.; Raghavachari, K.; Rendell, A. P.; Burant, J. C.; Iyengar, S. S.; Tomasi, J.; Cossi, M.; Millam, J. M.; Klene, M.; Adamo, C.; Cammi, R.; Ochterski, J. W.; Martin, R. L.; Morokuma, K.; Farkas, O.; Foresman, J. B.; Fox, D. J. *Gaussian 16*, Rev. A.03; Gaussian, Inc.: Wallingford, CT, 2016.

(69) Kresse, G.; Furthmüller, J. Efficient Iterative Schemes for Ab Initio Total-Energy Calculations Using a Plane-Wave Basis Set. *Phys. Rev. B* **1996**, *54*, 11169−11186.

(70) Coughlin, J. E.; Zhugayevych, A.; Wang, M.; Bazan, G. C.; Tretiak, S. Charge Delocalization Characteristics of Regioregular High Mobility Polymers. *Chem. Sci.* **2017**, *8*, 1146−1151.